Numerical simulations of direct liquid cooling of the end-windings of an electric machine

Adèle Poubeau, Guillaume Vinay, Breno Mendes Alves, Xiaohan Bai, Pierre Viot

International Journal of Heat and Mass Transfer 235 (2024) 126162

Contents lists available at ScienceDirect

International Journal of Heat and Mass Transfer

journal homepage: www.elsevier.com/locate/hmt

Numerical simulations of direct liquid cooling of the end-windings of an electric machine

Adèle Poubeau [a,*], Guillaume Vinay [b], Breno Mendes Alves [a], Xiaohan Bai [a], Pierre Viot [a]

[a] IFP Energies nouvelles, Institut Carnot IFPEN Transports Energie, 1 et 4 avenue de Bois-Préau, Rueil-Malmaison, 92500, France
[b] IFP Energies nouvelles, Institut Carnot IFPEN Transports Energie, Rond-point de l'échangeur de Solaize, Solaize, 69360, France

ARTICLE INFO

Keywords:
Volume of fluid
High Prandtl number
Liquid jet impingement
Partially wetting film
Electric machine cooling

ABSTRACT

The laminar two-phase flow associated with the liquid cooling of the end-windings of an electric machine by oil jets is investigated by means of 3D simulations using the Volume of Fluid (VoF) approach. The study focuses on the analysis and validation of flow hydrodynamics and heat transfer, which have rarely been studied in such depth to date for this type of configuration. Surface corrugations and rotor movements are neglected to reduce the physical complexity of the flow and limit computational time, thus making it possible to carry out a grid sensitivity analysis and a variation of oil properties. Using Adaptative Mesh Refinement (AMR) and a boundary-layer grid along the end-windings surface yields limited alteration of the steady film coverage and film Reynolds numbers when coarsening the grid. Regarding heat transfer, however, the large Prandtl numbers of the liquid ($100 < Pr < 400$) require fine cells at the wall (35 μm high for the conditions tested here) to achieve grid convergence, particularly in the jet impingement areas. Variations of liquid flow rate and oil properties are then carried out to identify key parameters in cooling, providing useful information for future simulations as well as optimization of such a system. The results show trends in film coverage that are consistent with previous studies in the literature: a wider film is obtained by increasing liquid flow rate or viscosity, or by decreasing surface tension or static contact angle. However, only an increase in flow rate or a decrease in static contact angle effectively enhance heat transfer (+78% in overall heat transfer with four times the oil flow rate and +100% for a decrease in contact angle from 120 to 10°). For the other cases, the loss in film cooling efficiency (due to a lower film Reynolds number), counterbalances the higher wet surface. An increase of 30% in heat transfer is found for a decrease in kinematic viscosity from 32 to 8.5 mm^2s^{-1}, while the variation of surface tension (from 0.02 to 0.04 $N.m^{-1}$) has a negligible effect. Over all parametric variations tested, the average film Reynolds does not exceed 30 (with a standard deviation of similar magnitude), with local values which do not exceed 100. Film height remains on average between 1.2 and 1.6 mm.

1. Introduction

Thermal management of electric machines is a major issue for increasing their power density. Components such as stator windings or rotor magnets are subject to high temperatures due to heat losses, which can cause irreversible degradation without any effective cooling system. Direct oil cooling architectures can complement more conventional approaches, such as a water jacket surrounding the stator, to ensure a sufficient cooling on every sensitive component, typically the end-windings, which are not in direct contact with the water jacket. In practice, Automatic Transmission Fluid (ATF) is used as coolant, as it is a di-electric fluid already present in the vehicle. Designing the best direct cooling architecture while ensuring machine compactness remains challenging. Various approaches have been investigated in previous experimental or numerical studies: rotating jets exiting from the hollow shaft [1–5], static impinging jets [3,6–9] or sprays [4,6,7,9,10]. All these architectures aim to form a film covering the stator end-windings as much as possible, offering the highest heat transfer, while reducing the pressure losses. The flow rate and temperature of the oil as well as its properties can also be optimized (for instance the viscosity [7]).

Experimentally, the evaluation of these systems relies mainly on local temperature measurements inside the end-windings. These experiments are complex and costly to set up, and offer only a partial thermal assessment of the machine. They are usually complemented by three-dimensional (3D) simulations. Computational Fluid Dynamics (CFD) is used to simulate the two-phase flow (oil and air) and estimate heat transfer at the end-windings surface. These simulations are weakly or strongly coupled to thermal simulations of the solid part of the machine

* Corresponding author.
E-mail address: adele.poubeau@ifpen.fr (A. Poubeau).

https://doi.org/10.1016/j.ijheatmasstransfer.2024.126162
Received 11 March 2024; Received in revised form 22 August 2024; Accepted 3 September 2024
Available online 11 September 2024

(using lumped parameter thermal networks [2] or finite element analysis (FEA) [3,4,8,11,12]) to obtain a complete 3D temperature map. Performing CFD simulations of this type of flow remains a challenge, primarily due to the complex, multi-scale physical phenomena involved in direct cooling, such as impinging jets on intricate surfaces and high-Prandtl partially wetting liquid film flow. This is why advanced modeling approaches need to be employed, that may require significant computational resources. Direct validations of the simulated flows remain rare and usually qualitative [6,9]: dedicated test benches with visual access and advanced optical techniques to characterize the liquid films are required. Local measurements of temperature in the machine (usually end-windings) have been used to validate the modeling approach [3,8,10,11]. However, this does not fully validate the flow, as simulated temperatures in the solid are subject to uncertainties arising from both fluid and solid models (the latter is particularly complex to implement, since it requires, among other things, to take into account the machine losses, the anisentropic conductivity of certain materials, and numerous contact resistances). This justifies a numerical study focusing solely on two-phase flow modeling, with the aim of analyzing and validating hydrodynamics and heat transfer. Full 3D CFD simulations of direct liquid cooling of end-winding have been carried out in few studies. In [8], Reynolds-Averaged Navier–Stokes Simulations (RANS) of a dozen oil jets impinging the hairpin end-windings and the stator of an electric machine were performed, coupled to a thermal model of the machine. Comparison to local measurements of temperature gave promising results, although the important assumption of a single-phase, turbulent flow was made. The Volume of Fluid (VoF) two-phase flow approach was used in [3], weakly coupled to a thermal model of the machine, to simulate a cooling configuration of the end-windings combining rotating and impinging jets. The complex structure of the end-windings and the rotating geometry effect are accounted for in the model, resulting in a grid of 117 million cells (for the fluid phase only), requiring several days of simulations for a single operating point. Results of this comprehensive simulation compare well to local measurements of temperature. The same authors extended this work to study the cooling induced by 25 sprays of oil on the end-windings and rotor drum [4]. These two studies, although very comprehensive in their consideration of physical phenomena, lack details in the numerical setup: for instance the choice of grid cell size in the liquid phase, or the approach to solve heat transfer (use of a wall law or full resolution of the temperature field within the liquid film?) are not explained, whereas they could serve as guidelines for future numerical studies. Similarly, no grid sensitivity study was presented, while they could enhance the robustness of the numerical results. A more in-depth study of the two-phase flow was performed in [5]: also using the VoF approach, RANS and Large-Eddy Simulations (LES) of a scaled rotor end ring, cooled by two rotating oil jets exiting the rotor shaft, were carried out. The jet breakup and impingement, film coverage and heat transfer were analyzed, and their sensitivity to the numerical approach (RANS or LES) or to the grid was investigated. If the jet was little altered by the variations tested, the impingement area and the subsequent film coverage seemed to require a high resolution method, due to the turbulence induced by the rotating jets. The authors notably suggest the coupling of the VoF model to a Lagrangian model to better account for the jet break-up due to the rotor spinning. A convergence in heat transfer was also achieved for a fine grid in the film (less than 50 μm).

The present study aims to follow a similar approach to that presented in [5], considering a cooling by dripping nozzles. This system consists in a few oil jets impinging the top of the end-windings at low velocities. It proved to be one of the most efficient approaches [6,7,9], enabling a significant film coverage while limiting the pressure loss. The objective of the present study is twofold. First, Volume of Fluid (VoF) simulations of a full-scale end-windings cooled by five laminar impinging jets forming a film are carried out. Compared to previous numerical works, the setup is simplified: no thermal model of the electric machine, no rotation of the rotor and a smooth end-windings surface are considered. This breaks down the excessively complex physical phenomena involved into a simpler case which can be simulated with a reasonable computational time, allowing to conduct a grid sensitivity analysis. The latter is based on a detailed hydrodynamic and thermal film characterization which, to the best of the author's knowledge, has never been conducted in the numerical studies listed previously; its objective is to propose best practices regarding grid definition, along with validation criteria for the flow, especially when direct experimental measurements are unavailable. In a second phase, the numerical setup offering the best compromise between accuracy and computational time is used to evaluate the sensitivity of the cooling system to the oil flow rate and to certain oil properties. These properties either exhibit significant variability among different oils (e.g. viscosity [7]), or are rarely known with accuracy (e.g. surface tension or static contact angle, whose values are very rarely provided in previous studies). Again, to the best of the author's knowledge, such an extensive numerical sensitivity study has never been carried out in conditions as close as possible to a realistic industrial setup. The aim is to identify the first-order oil properties in the end-windings cooling, and the physical mechanism involved.

Obviously, the simplifying assumptions adopted in this study preclude any general conclusion about the oil flow encountered in an actual electric machine directly cooled by oil. A numerical study including both rotor movement and end-winding roughness is the authors' final objective but was considered too ambitious at first (both in terms of modeling and computational efforts involved). Instead, by proposing a first comprehensive analysis of this type of flow (even simplified), together with a grid strategy allowing for the prediction of heat transfer, the present work aims at paving the way towards fully realistic and validated simulations of end-windings cooled by oil jets.

Finally, it should be noted that the present work is a continuation of previous simulations of high Prandlt number liquid jets impacting a heated flat plate [13]. The same numerical approach, which has been validated by measurements of mean surface heat transfer in [13], is applied for these new simulations.

The following study is organized as follows: the first section is dedicated to the numerical setup, with a description of the electric machine and of its cooling architecture, on which the simulations are based, followed by details on the computational domain, the operating conditions, the grid strategy and the numerical methods. The grid sensitivity analysis is described in Section 3, which includes an analysis of heat transfer in the jet impingement areas and a statistical description of the film. Finally, Section 4 studies the impact of oil flow rate, oil viscosity, surface tension and static contact angle on the film hydrodynamics and heat transfer.

2. Numerical setup

2.1. Description of the electric machine

An electric machine (Fig. 1(a)), representative of a commercial traction electric machine, has been specifically designed to experimentally evaluate the efficiency of direct oil cooling [7]. In addition to a conventional cooling system using a water jacket surrounding the stator, an oil circuit has been integrated, whose modular design enables various oil injection architectures to be tested: flat jet nozzle, full cone nozzle, impinging circular jets, etc. The water and oil circuits have been instrumented with pressure and temperature sensors, and a series of thermocouples has been integrated into the stator windings, allowing a precise thermal evaluation of the machine. Tests have been performed for four oils at different injection temperatures, combined or not to water cooling, during no-load and load tests at different rotational speeds (up to 14,000 rpm). A significant decrease in the coil end-windings temperature could be observed when adding a direct cooling system to the conventional water jacket, proving the interest

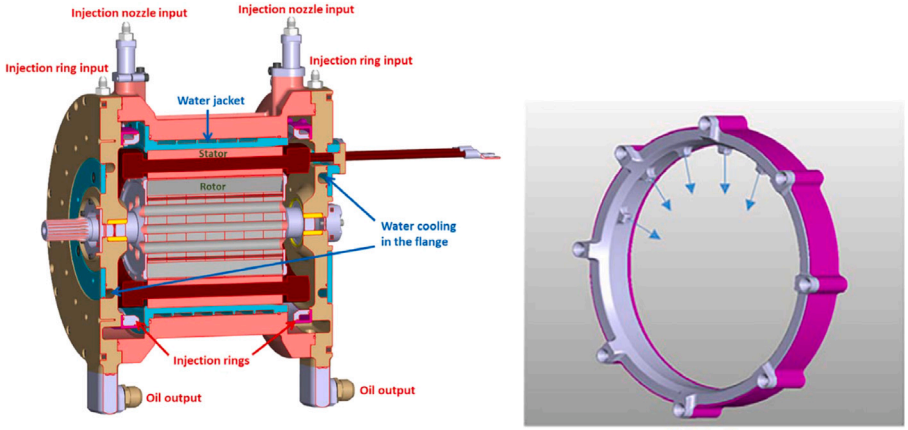

(a) (b)

Fig. 1. General architecture of the electric machine (a) and schematic of the oil cooling system considered in the present study (b).
Source: From [7].

of the approach (detailed results can be found in [7]). The present study focuses on the dripping architecture, found to be one of the most efficient cooling systems, represented in Fig. 1(b). It consists in a ring, placed around the end-windings, with 5 outlet holes of diameter 3.2 mm located on top. The flow rate ranges from 120 to 480 l/h, allowing the formation of 5 impinging jets forming a film on the end-windings. Although the present study focuses exclusively on the flow resulting from the direct liquid cooling, for which no dedicated experimental characterization could be carried out, the simulation of this particular configuration nevertheless has two advantages. First, it is representative of an actual electric machine, meaning that even with the simplifying assumptions considered here (detailed in the next section), the numerical setup remains realistic in terms of geometry and operating conditions. Secondly, in the future, the present simulations can be strongly or weakly coupled to thermal simulations of the machine, allowing the comparison of resulting temperatures in the solids to the thermocouples measurements. Consequently, the experimental data here are mainly used as inputs for a realistic numerical setup. Some purely qualitative comparisons between experimental and numerical results are proposed for the variations of oil flow rate (Section 4.1) and viscosity (Section 4.2). However, the validation of the present numerical approach relies mainly on the grid sensitivity study and the subsequent flow analysis described in Section 3.

2.2. Computational domain and operating conditions

Given the complexity of the flow and the relatively large scale of the machine, a few simplifying assumptions are adopted to enable a large number of simulations to be carried out (including a grid sensitivity analysis and a variation of the operating conditions) while maintaining a reasonable computational time. First, the computational domain is reduced to one side of the machine. Secondly, the potential interactions between the liquid film and the air entrained by the rotor are neglected. The rotor is then kept in a fixed position, and the flow through the air gap is not considered. Thirdly, the oil ring (shown in Fig. 1(b)) is not included: a dedicated, 3D single-phase simulation of the flow through the oil ring was carried out beforehand, in order to determine the distribution of the oil flow rate in the various nozzle exits, which are then used as the inlet conditions of this setup. Finally, the effect of the corrugated surface of the end-windings on flow hydrodynamics and heat transfer is not studied here. Indeed, recent works showed that a very fine grid resolution seems necessary to correctly predict heat transfer for this type of surface [14]. These requirements are not realistically compatible with the spatial scales considered in the present study, therefore the surface is considered fully smooth. The computational domain is represented in Fig. 2(a): a symmetry condition is applied on the plane $y = 0$, reducing even further the domain. The three injectors (including the one in the symmetry plane) are located on top of the end-windings. Film hydrodynamics and heat transfer are studied on the surface of the end-windings, represented in blue in Fig. 2(b). To allow a local characterization of the film, this surface is decomposed into 3 parts: the outer, inner and side surface, whose respective areas are indicated in Table 1.

Initially, the domain is filled with air at temperature $T_a = 20$ °C and pressure $P_a = 1$ bar. No-slip and isothermal boundary conditions are imposed on all walls. Specifically, the surface temperature of the end-windings is fixed at $T_s = 67$ °C, which is coherent with the temperature measurements in [7]. The temperature of the other walls (rotor and end-shield) is fixed at 40 °C. This value was chosen in the absence of temperature measurement, however it should be noted that hydrodynamics and heat transfer are only studied on the end-windings, and should be little affected by the flow over the rotor and/or the end-shield. These values of surface temperature are kept constant in all simulations presented in this study. An outlet boundary condition is placed at the bottom of the domain, as indicated in Fig. 2(a). Regarding the conditions of oil injection, as mentioned previously, they were determined by dedicated simulations of the oil ring (not detailed here). The analysis of these simulations showed that, due to the geometry of the oil ring and the position of its oil inlet, the flow rate of the central injector (no. 1 in Fig. 2(a)) is nearly 1.2 times larger than those of the side injectors (no. 2 and 3 here). This difference was reproduced in the present simulations. For the reference flow rate $\dot{v} = 2.85$ l min^{-1} (value corresponding to the cooling of one side of the machine), the flow rates imposed for the central and side injectors are 0.65 and 0.55 l min^{-1}, respectively. The oil temperature at the inlet is fixed at $T_f = 40$ °C. For all simulations, the oil properties, including thermal conductivity, heat capacity and density are held constant and chosen at the fluid temperature at the inlet T_f: $k_f = 0.137$ W(m K)$^{-1}$, $c_{p,f} = 2090$ J (kg K)$^{-1}$ and $\rho_f = 814$ kg m^{-3}. A variation of the oil viscosity ν_f, surface tension σ, static contact angle θ_s as well as oil flow rate $\dot{v}$ is carried out to study their impact on flow hydrodynamics and heat transfer (see Section 4). Values are listed in Table 2, where conditions for the reference case (used for the grid sensitivity analysis in Section 3) are denoted by an asterisk. The wide range of simulated viscosities is representative of the oils tested in [7]. The impact of the variation of viscosity with temperature is also tested, using Walther's equation [15] to estimate a realistic relation $\nu_f = f(T)$:

$$\ln\ln(\nu_f + 0.7) = m \ln T + C \tag{1}$$

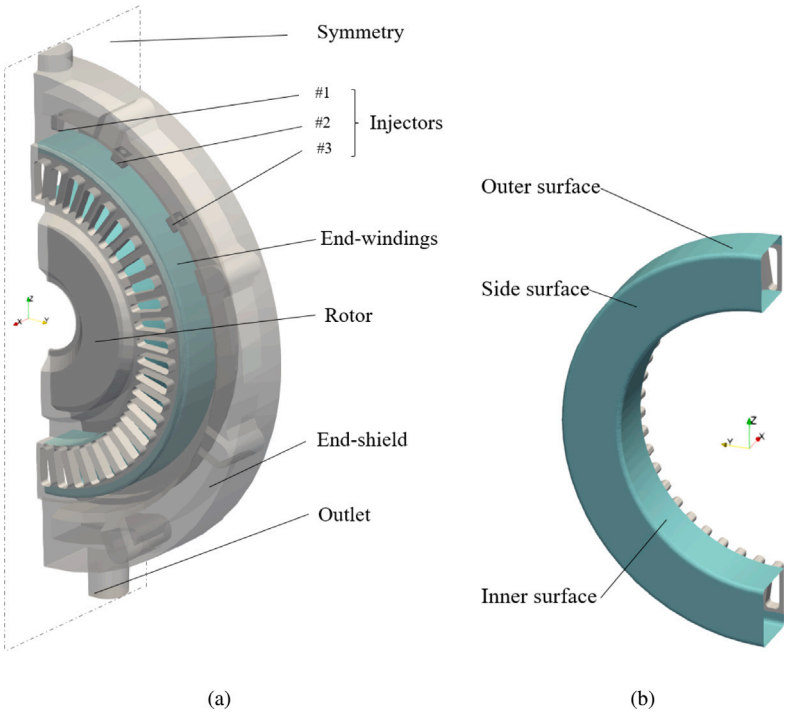

Fig. 2. Computational domain (a) and decomposition of the simplified end-windings surface (b) (in blue: location of the boundary-layer grid). (For interpretation of the references to color in this figure legend, the reader is referred to the web version of this article.)

Table 1
Surface area of the end-windings parts (in cm^2).

S_{outer}	S_{inner}	S_{side}	S_{total}
85.2	52.5	70.3	208.0

where $m = -3.146$ (value taken from [16] for automatic transmission fluid) and $C = 19.092$, imposed so that $\nu_f(T = T_f) = 15\ mm^2\ s^{-1}$. Oil surface tension and static contact angle have rarely been characterized in previous experimental or numerical studies in the context of electric machine cooling; it is therefore interesting to study their impact on the flow. The variation of the surface tension coefficient remains in the order of magnitude of values given in [16] for automatic transmission fluid. Regarding the static contact angle, five values are tested, from hydrophilic ($\theta_s = 10°$) to hydrophobic ($\theta_s = 120°$) angles.

Impinging jets are usually characterized by their Reynolds number Re_j, based on the jet bulk velocity u_f and the nozzle diameter d. Here, the bulk velocity is estimated from the fluid mass flow rate $\dot{m}$:

$$Re_j = \frac{u_f d}{\nu_f} = \frac{4\dot{m}}{\pi \mu_f d} \tag{2}$$

The Prandtl number of the fluid, the ratio of momentum diffusivity to thermal diffusivity, is defined as follows:

$$Pr = \frac{c_{p,f}\,\mu_f}{k_f} \tag{3}$$

For the conditions of flow rate and viscosity tested in the present study, Re_j ranges between 135 and 805, and Pr between 107 and 396 (see Table 3).

2.3. Grid definition

The computational grid should be able to capture the position of the liquid/gas interface while also ensuring a sufficient resolution within the liquid film thickness to accurately predict both hydrodynamics and heat transfer. In the computational domain, the grid is automatically discretized using the cut-cell Cartesian method implemented in CONVERGE [17]. The Adaptative Mesh Refinement (AMR) approach is used to dynamically and automatically refine the grid at the liquid/gas interface, i.e. in the regions of high gradients of void fraction α. Three different cell sizes of AMR are tested in Section 3 for the reference operating conditions: 0.2, 0.3 and 0.4 mm. In the outlet region of the computational domain, under the end-windings, the AMR cell size is increased by a factor 2 to limit the total number of cells. In addition to the AMR, a boundary-layer (b.–l.) grid is imposed on most of the end-windings surface (blue area in Fig. 2(b)). Four b.–l. grids are tested in Section 3 for the reference operating conditions, with the objective to find the minimal resolution required for accurate predictions of flow hydrodynamics and heat transfer. The high Prandtl numbers of the studied flows mean that the thermal boundary layer thickness δ_t is smaller than the hydrodynamic layer thickness δ: solving heat transfer is more constraining in terms of grid resolution. The minimum cell size at the wall Δ_{min} and total number of cells within Δ_{tot} vary as detailed in Table 4. For the 4 grids, the resolution tangential to the wall is 0.5 mm and the total height of the b.–l. grids Δ_{tot} remains constant, at 0.4 mm (except for grid $\Delta_{min} = 300$ µm, which contains only one cell within Δ_{tot}). The finest b.–l. grid, $\Delta_{min} = 35$ µm, aims at fully solving heat transfer in the entire flow, including the jet stagnation zones, where heat transfer are maximum (so where δ_t is the thinnest) [13,18,19]. An analytical approach [20] correlates the thermal boundary layer thickness in the stagnation zone $\delta_{t,stagn}$ with the nozzle diameter d, Re_j and Pr numbers:

$$\delta_{t,stagn} \sim d\, Re_j^{-1/2} Pr^{-1/3} \tag{4}$$

Table 2
Variation of fluid properties and flow rate.

Parameter	Values
$\dot{v}$ ($l\,min^{-1}$)	1.8, 2.85[a], 5, 8
ν_f ($mm^2\,s^{-1}$)	8.5, 15[a], 32, $\nu_f = f(T)$
σ ($m\,Nm^{-1}$)	20, 25, 30[a], 35, 40
θ_s (°)	10, 30[a], 60, 90, 120

[a] Reference case.

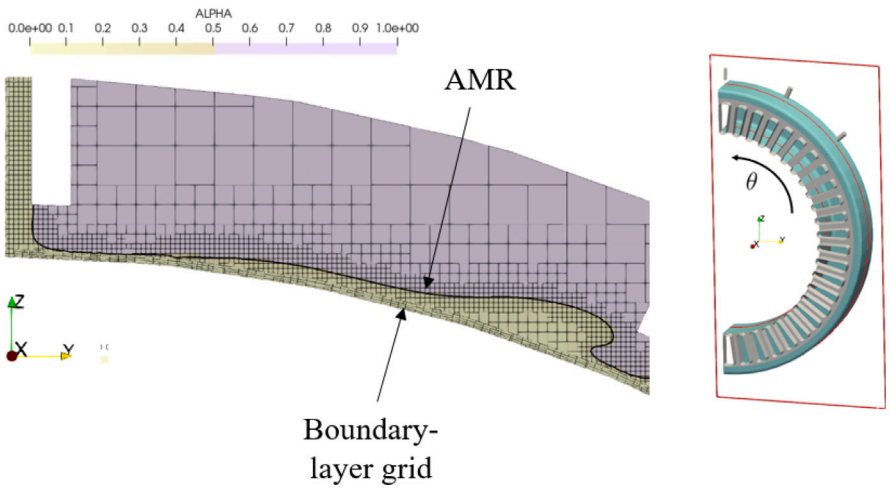

Fig. 3. Slice of the computational domain in $x = 0$, passing through the liquid jet centers (slice location is depicted on the right), showing the grid in the liquid film between jets no. 1 and 2. The black line represents the position of the liquid/gas interface (iso-contour $\alpha = 0.5$).

Table 3
Values of Pr number, Re_j number and $\delta_{t,stagn}$ for the variations of viscosity and liquid flow rates.

Parameter		Pr	Jet # 1		Jet # 2	
			Re_j	$\delta_{t,stagn}$ (μm)	Re_j	$\delta_{t,stagn}$ (μm)
$\dot{v}$ (l min^{-1})	1.8	186.2	181.3	41.6	153.4	45.2
	2.85[a]		287.0	33.1	242.8	36.0
	5		503.5	25.0	426.0	27.2
	8		805.6	19.7	681.6	21.5
ν_f (mm^2 s^{-1})	8.5	106.6	508.3	29.9	430.1	32.5
	15[a]	186.2	287.0	33.1	242.8	36.0
	32	396.1	134.9	37.5	114.1	40.8

[a] Reference case.

Table 4
Variation of b.-l. grid definitions.

Δ_{min} (μm)	ER	Δ_{tot} (mm)	No. of cells within Δ_{tot}	Tot. no. of cells in the b.-l. grid
35	1.4	0.38	5	737,000
100	1.14	0.4	4	637,000
200	1	0.4	2	436,000
300	1	0.3	1	334,000

The numerical evaluation of Eq. (4) for the operating points in Table 2 corresponding to the variations of liquid flow rate and viscosity is given in Table 3: $\delta_{t,stagn}$ ranges between 19.7 and 45.2 μm. A grid sensitivity analysis carried out in [13] showed that accurate predictions of heat transfer in the impinging jet area are achieved if at least one grid cell is imposed within $\delta_{t,stagn}$. If the height of the first cell Δ_{min} is 2 or 3 times $\delta_{t,stagn}$, heat transfer in the stagnation zone are expected to be under-predicted, but the error in heat transfer prediction averaged over a surface of radius $3d$ from the impinging point should be limited (less than 10%). Based on these conclusions, the finest grid should adequately solve heat transfer for the reference conditions, even for the stagnation zone, as $\Delta_{min} = 35$ μm is close to $\delta_{t,stagn}$ (33.1 μm for jet 1 and 36 μm for jets 2 and 3). Secondly, the error in heat transfer prediction induced by the grid $\Delta_{min} = 100$ μm should not exceed 10% on the reference case. This aspects, as well as the hydrodynamics and heat transfer obtained for the two other b.–l. grids, are evaluated in Section 3. Finally, on the side of the end-windings without b.–l. grid (gray areas in Fig. 2), a fixed cell size of 300 μm was imposed close to the wall, with a first off-wall cell of 150 μm height, to ensure relevant hydrodynamics and heat transfer predictions.

The grid strategy is illustrated in Fig. 3 which shows, for the portion of film between jets no. 1 and 2, the grid refinement at the gas/liquid interface for an AMR cell size of 0.3 mm, and the b.–l. grid with $\Delta_{min} = 100$ μm.

2.4. Numerical methods

The two-phase flow is modeled by the VoF approach [21]. Both phases are considered incompressible and share a mass, momentum and energy equation. Specifically, the momentum equation accounts for the gravitational acceleration and the surface tension effects:

$$\rho\left[\frac{\partial u_i}{\partial t} + \frac{\partial (u_j u_i)}{\partial x_j}\right] = -\frac{\partial p}{\partial x_i} + \frac{\partial}{\partial x_j}\left[\mu\left(\frac{\partial u_i}{\partial x_j} + \frac{\partial u_j}{\partial x_i}\right)\right] + \rho g_i + \sigma\kappa n_i \tag{5}$$

where g is the gravitational acceleration, σ the surface tension of the liquid, κ the curvature and $\mathbf{n}$ the unit normal to the interface. In addition to the mass, momentum and energy, the volume fraction α is also transported to describe the evolution of the free surface in time:

$$\frac{\partial \alpha}{\partial t} + u_j \frac{\partial \alpha}{\partial x_j} = 0 \tag{6}$$

The value of α indicates the presence ($\alpha = 1$) or absence ($\alpha = 0$) of gas in the control volume. Finally, the following constitutive relations between material properties are considered:

$$\rho = \rho_g \alpha + \rho_f (1 - \alpha) \tag{7}$$

$$\mu = \mu_g \alpha + \mu_f (1 - \alpha) \tag{8}$$

where indices g and f represent the gas and liquid properties, respectively. Eqs. (5)–(8) are solved in the finite-volume CFD code CONVERGE (v3.1.6). Considering the low values of Reynolds number encountered, no turbulence model was used. A pressure-based PISO algorithm (with a tolerance fixed at 10^{-3}) is applied, and pressure, momentum and energy terms are discretized with a second-order upwind scheme. Time step is limited by the maximum convection CFL number, fixed at 0.75 for all cases. To discretize the convective term in the transport equation of α (Eq. (6)), the High-Resolution Interface Capturing (HRIC) scheme is used [22].

The calculation of the surface tension term in Eq. (5) is based on the Continuum Surface Force (CSF) model of Brackbill [23]. The vector normal to interface is then written

$$n_i = \frac{\partial \alpha}{\partial x_i}\left(\left|\frac{\partial \alpha}{\partial x_i}\right|\right)^{-1} \tag{9}$$

and curvature κ:

$$\kappa = -\frac{\partial n_i}{\partial x_i} \tag{10}$$

To compute $\mathbf{n}$ and κ in the contact line cell, a static contact angle θ_s is specified. The surface normal in the contact line cell is then written

$$n_i = n_{w,i}\cos(\theta_s) + t_{w,i}\sin(\theta_s) \tag{11}$$

where $n_{w,i}$ and $t_{w,i}$ are the unit vectors normal and tangential to the wall, respectively.

This numerical approach has been validated for simulations of falling liquid films with side contact lines on a flat plate, for which experimental characterization exists [24]. Results are presented in Appendix.

3. Grid sensitivity analysis for hydrodynamics and heat transfer predictions

3.1. Simulation convergence and flow visualization

A preliminary analysis of the flow features and convergence is conducted for the reference operating conditions, with intermediate AMR cell size (0.3 mm) and b. –l. grid (Δ_{min} = 100 µm). Fig. 4 depicts the temporal evolution of wet surface ratio ξ, defined as the surface of end-windings covered by the oil film (S_{film}), divided by the total surface (S_{total}):

$$\xi = \frac{S_{film}}{S_{total}} \tag{12}$$

This ratio is also computed for the three parts composing the end-windings, depicted in Fig. 2(b). At least 4 s of physical time seem necessary to establish the film formation over the end-windings. At t = 5 s, the film covers 75% of the end-windings surface, with local variations: 92% of the inner surface is covered by oil, against 59% of the side surface. The outer surface, which included the jet impinging area, is covered at 77%. These percentages are illustrated in Fig. 5(a), depicting the film covering the end-windings (represented by an iso-contour of void fraction α = 0.5). Jet interactions and hydrodynamics waves are visible on the outer surface. As the film flows down the end-windings, it gets detached and drips to the outlet. The rotor gets partially covered by the film, but this aspect is not studied further in the present work. Heat transfer on the end-windings due to both air and liquid film cooling is characterized by the local heat transfer coefficient (HTC) h, defined as

$$h = \frac{\dot{q}}{T_s - T_f} \tag{13}$$

where $\dot{q}$ is the heat flux. Considering that T_s and T_f are constant values in the present simulations, h is directly proportional to $\dot{q}$. The distribution of h over the end-windings surface is shown in Fig. 5(b) (in logarithmic scale). A peak of HTC, above 1500 W K^{-1} m^{-2}, is visible in the jet impingement areas, under the injectors. Elsewhere in the film, values of HTC range mostly between 300 and 600 W K^{-1} m^{-2}. The surface-averaged HTC is calculated as follows:

$$\overline{h} = \frac{\overline{\dot{q}}}{T_s - T_f} \tag{14}$$

In order to assess the cooling efficiency of the liquid film only, surface-averaged HTC is also computed on the wet surface:

$$\overline{h}_{film} = \left.\frac{\overline{\dot{q}}}{T_s - T_f}\right|_{\alpha \leq 0.5} \tag{15}$$

The temporal evolution of $\overline{h}$ and $\overline{h}_{film}$ for the different parts of the end-windings is represented in Figs. 6(a) and 6(b) respectively. As for the wet surface ratio, steady-state is reached after 4 s. At t = 5 s, $\overline{h}$ = 365 W K^{-1} m^{-2} and $\overline{h}_{film}$ = 457 W K^{-1} m^{-2} over the end-windings surface. The film covering the outer surface has the highest

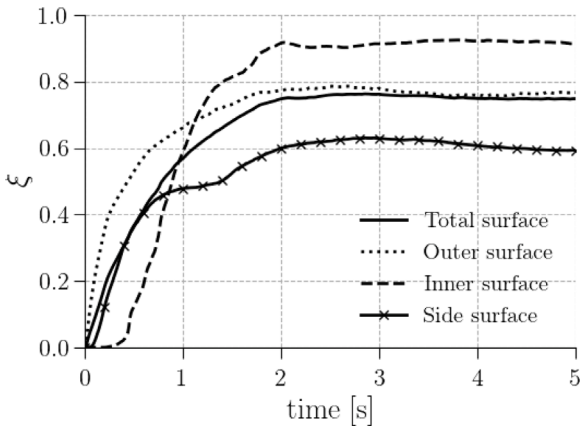

Fig. 4. Temporal evolution of wet surface ratio for each part of the end-windings (ref. operating conditions, AMR = 0.3 mm, b.–l. grid with Δ_{min} = 100 µm).

cooling efficiency (due the contribution of the jets) with $\overline{h}_{film,outer}$ = 560 W K^{-1} m^{-2}, which is 22% higher than $\overline{h}_{film}$. The share of liquid cooling due to the outer surface on the total liquid cooling can be estimated by the following equation:

$$\frac{q_{film,outer}}{q_{film}} = \frac{\overline{h}_{film,outer}\,\xi_{outer}\,S_{outer}}{\overline{h}_{film}\,\xi\,S_{total}} \tag{16}$$

where $q_{film,outer}$ and q_{film} are the heat transfer rates due to the film on the outer and total surfaces of end-windings, respectively. Eq. (16) gives 0.52, meaning the film on the outer surface is responsible for 52% of the film cooling over the end-windings, while its area represents 40% of the total surface, covered at 77% by film. The cooling efficiency of both inner and side surfaces are similar ($\overline{h}_{film}$ = 397 and 377 W K^{-1} m^{-2}, respectively), but the lower wetting ratio of the side surface (59%) entails lower HTC $\overline{h}$ on this surface, as visible in Fig. 6(a). The observations made in this section regarding the surface wetting and heat transfer are only valid for the reference operating point, and vary with the flow rate and liquid properties, as seen in Section 4.

Note: the resulting return time for 5 s of simulation is about 1.5 day on 4 nodes (8 CPUs Intel Skylake G-6140, 144 cores), representing 5415 CPU hours.

3.2. Impact of liquid/gas interface resolution

The impact of AMR cell size, allowing a refinement of the grid at the liquid/gas interface of the flow, is assessed for the reference operating conditions. The numerical setup is similar to that described in Section 3.1, with the b.–l. grid of minimal resolution Δ_{min} = 100 µm imposed on the end-windings surface. The objective is twofold: ensuring a minimal resolution within the film thickness (which is necessary to compare heat transfer predictions) and avoiding any impact of the AMR cell size on the triple line modeling by keeping the same cell size at the wall. Three cell sizes are tested: 0.2, 0.3 and 0.4 mm (the case with 0.3 mm corresponds to the simulation presented in the previous section). Results are summarized in Table 5. The impact of the resolution at the interface seems negligible on the wet surface ratio ξ. Regarding heat transfer, a slight decrease in $\overline{h}$ and $\overline{h}_{film}$ can be noted when decreasing the cell size. However, the additional computational time induced by the finest grid is prohibitive: 15,500 CPU hours for 5 s of physical time, which represents a return time of 4.5 days using 4 nodes. For the rest of the study, the AMR cell size of 0.3 mm is chosen, as it gives a relatively small error compared to the finest grid (+1.7% on $\overline{h}$ and +4.6% on $\overline{h}_{film}$) while allowing a manageable computational time.

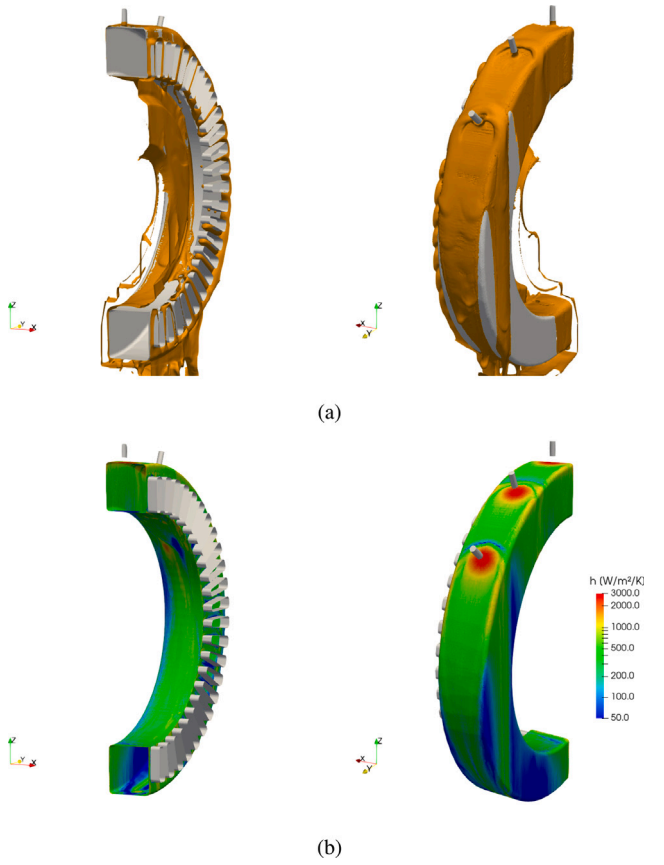

Fig. 5. Iso-contour of void fraction $\alpha = 0.5$ (a) and surface of end-windings colored in HTC (b) at $t = 5$ s (ref. operating conditions, AMR = 0.3 mm, b.–l. grid with $\Delta_{min} = 100$ µm). Injectors are represented in gray to facilitate the understanding. (For interpretation of the references to color in this figure legend, the reader is referred to the web version of this article.)

Table 5
Wet surface ratio and surface-averaged HTC over the end-windings, tot. number of cells in the computational domain (at $t = 5$ s) and CPU hours for 5 s of simulation for the variation of AMR cell size.

AMR cell size [mm]	0.2	0.3	0.4
ξ	0.77	0.75	0.77
HTC [W K^{-1} m^{-2}]			
$\overline{h}$	359	365	378
rel. diff. to AMR = 0.2 mm [%]	–	+1.7	+5.3
$\overline{h}_{film}$	437	457	469
rel. diff. to AMR = 0.2 mm [%]	–	+4.6	+7.3
Numerical aspects			
No. cells [million]	7.2	3.0	1.8
CPU hours	15,500	5415	4280

3.3. Impact of boundary-layer grid resolution

The resolution within the film thickness, and particularly the hydrodynamic and thermal boundary layers, is mostly determined by the b.–l. grid. The variation of b.–l. grid described in Table 4 is carried out keeping a fixed AMR cell size at 0.3 mm and for the reference operating conditions. Regarding the film hydrodynamics, there is a strong transient effect for the finest grid ($\Delta_{min} = 35$ µm), visible in Fig. 7, depicting the temporal evolution of the wet surface ratio over the end-windings. If the steady-state is only slightly impacted, nearly 10 s of physical time are required to converge the simulation, which largely doubles the computational time, as shown in Table 6. The contact line modeling approach followed here may explain this behavior, since it

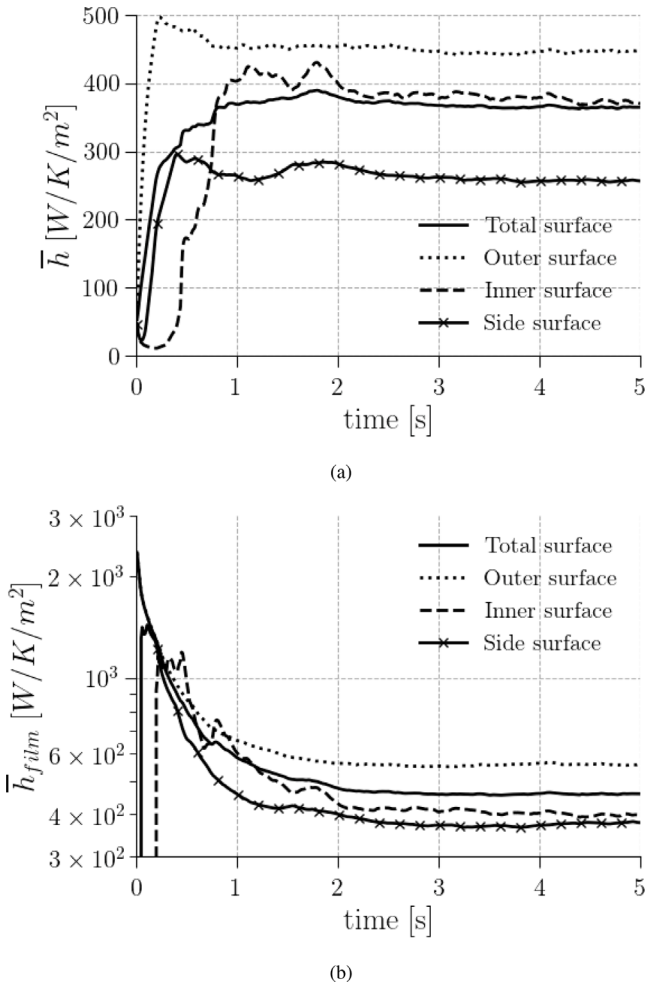

Fig. 6. Temporal evolution of $\overline{h}$ (a) and $\overline{h}_{film}$ (b) for each part of the end-windings (ref. operating conditions, AMR = 0.3 mm, b.–l. grid with $\Delta_{min} = 100$ µm).

is based on a static contact angle model with a no-slip condition on the wall, which is known to cause the viscous stresses at the contact line to diverge when refining the grid size [25–27]. In these conditions, previous simulations of a droplet spreading on a wall [27] showed a strong sensitivity of the spreading time of the drop to the grid, even if the final state was not impacted. The use of a dynamic contact angle model, like Cox's [28], could mitigate this grid sensitivity [27], possibly in conjunction with a Navier slip model [26]. These aspects deserve a dedicated numerical study, with relevant experimental data for comparison and validation. However, as the effects associated with contact line modeling appear to influence transient behavior without altering the final state, we consider these effects to be negligible in the context of our analysis.

The ratio of wet surface ξ tends to decrease as the grid coarsens (from 0.77 down to 0.68 for $\Delta_{min} = 200$ µm according to Table 6). This decrease can be mostly attributed to the side surface of the end-windings (from 0.72 down to 0.43), and is even noticeable in Fig. 8 depicting the film. An even finer grid may be needed to model the film on this surface, perhaps due to the thinner film thickness on this location (see Section 3.5).

Regarding predictions of heat transfer, values of $\overline{h}$ and $\overline{h}_{film}$ tend to decrease as the grid is refined (see Table 6). The b.–l. grid $\Delta_{min} = 100$ µm gives very close predictions to the finest grid $\Delta_{min} = 35$ µm, with a relative difference of 6 and 8% for $\overline{h}$ and $\overline{h}_{film}$, respectively. This difference gets larger than 20% for the two coarsest b.–l. grids. With a small error in film covering and surface-averaged heat transfer, the

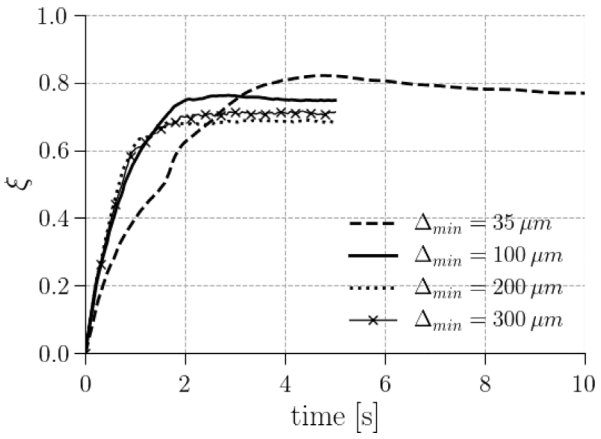

Fig. 7. Temporal evolution of wet surface ratio for 4 b.–l. grids (ref. operating conditions, AMR = 0.3 mm).

Table 6
Wet surface ratio and surface-averaged HTC over the end-windings, tot. number of cells in the computational domain (at $t = 5$ s) and CPU hours for the variation of b.-l. grid.

Δ_{min} [μm]	35	100	200	300
Wet surface ratio				
ξ	0.77	0.75	0.68	0.71
ξ_{side}	0.72	0.59	0.50	0.43
HTC [W/K/m^2]				
$\overline{h}$	344	364	412	451
rel. diff. to $\Delta_{min} = 35$ μm [%]	–	+6	+20	+31
$\overline{h}_{film}$	424	457	547	546
rel. diff. to $\Delta_{min} = 35$ μm [%]	–	+8	+29	+29
$\overline{h}_{film}$ (outer surf., $z \geq 0$)	693	737	760	681
rel. diff. to $\Delta_{min} = 35$ μm [%]	–	+6	+10	−2
Numerical aspects				
No. cells [million]	3.3	3.0	2.8	2.7
CPU hours (5 s)	6200	5415	4600	4600
CPU hours (10 s)	12,900	–	–	–

grid $\Delta_{min} = 100$ μm seems to give results comparable to the finest grid, for half the computational time. Further local, quantitative comparisons are carried out in Sections 3.4 and 3.5 to confirm this first observation.

3.4. Study of heat transfer in the jet impingement areas

As shown in Fig. 5(b), maximum values of HTC are reached in the jet impingement areas, where thermal boundary layer thickness δ_t is at a minimum. In this area, heat transfer predictions are particularly sensitive to the b.–l. grid. This is illustrated in Fig. 9, showing the evolution as a function of θ of local HTC h in the vicinity of jet no. 2 impingement area, in the plane $x = 0$ (plane and angle θ are depicted in Fig. 3). To ease interpretation, an offset $\theta_2 = 1.13$ rad is applied to the x-axis, corresponding to the location of stagnation point of jet no. 2. Peak value of h increases as the grid gets finer, with a factor larger than 5 between the coarsest and the finest grids. At this location, δ_t has reached a minimum, and only the finest grid offers enough cells at the wall for an acceptable resolution of δ_t and therefore of heat transfer, as explained in more details at the end of this section. To validate the predictions of grid $\Delta_{min} = 35$ μm, previous correlations for stagnation zone Nusselt number Nu_0, derived from fully resolved numerical simulations of impinging jets in similar ranges of Re_j and Pr numbers [13], can be applied. The following correlation was obtained:

$$Nu_0 = 1.287 Re_j^{0.49} Pr^{1/3} \tag{17}$$

where $Nu_0 = h_0 d / k_f$ (h_0 being the value of h at the stagnation point). For jet no. 2, Eq. (17) gives $h_0 = 4900$ W m^{-2} K^{-1}, based on values of Re_j and Pr given in Table 3. For the finest b.–l. grid $\Delta_{min} = 35$ μm, a similar value is obtained ($h_0 = 5500$ W m^{-2} K^{-1}). This suggests that this grid may be fine enough to predict heat transfer on the jet impingement areas, and therefore on the entire end-windings.

If the three coarser grids entail a considerable error in the prediction of maximum HTC, this is not the case for surface-averaged HTC. Table 6 lists values of $\overline{h}_{film}$ for the upper part of the outer surface ($z \geq 0$), which includes all jet impingement areas. This zone is fully covered by the film for all four b.–l. grids (so $\overline{h} = \overline{h}_{film}$), which rules out any difference in heat transfer between them due to a change in ξ. For grids $\Delta_{min} = 100$ and 200 μm, $\overline{h}_{film}$ is over-estimated by only 6 and 10%, respectively, compared to $\Delta_{min} = 35$ μm. This over-estimation as the grid coarsen, while maxima of HTC are actually under-estimated, can be explained with the example of jet no. 2 in Fig. 9. For grid $\Delta_{min} = 100$ μm, heat transfer are over-estimated for $0.04 < |\theta - \theta_2| < 0.1$ compared to the finest grid, before reaching similar values for $|\theta - \theta_2| \geq 0.1$. In terms of impact on the surface-averaged heat transfer, this local over-estimation of heat transfer prevails over the under-prediction of the peak of HTC. As for the similar HTC for $|\theta - \theta_2| \geq 0.1$ between the two grids, it suggests that grid $\Delta_{min} = 100$ μm is able to predict heat transfer in the film away from the stagnation zone. The grid $\Delta_{min} = 200$ μm systematically over-predicts heat transfer in the film for $|\theta - \theta_2| > 0.06$ in Fig. 9, which explains the even larger over-prediction of $\overline{h}_{film}$. The trend changes with grid $\Delta_{min} = 300$ μm, which is too coarse to predict any local increase in h due to the impinging jet. On average, this deficit in cooling is cancelled by the over-prediction of h further in the film for $|\theta - \theta_2| > 0.1$, leading to the similar predictions of $\overline{h}_{film}$ as for the finest grid. In conclusion, only the finest b.–l. grid may be able to predict the peak of heat transfer in the jet stagnation zone. However, as this area represents a limited amount of the total heat transfer, the coarser grid $\Delta_{min} = 100$ μm offers very similar results in terms of surface-averaged HTC, with a seemingly good resolution of the heat transfer away from the impingement zone, for a reduced computational cost.

For further understanding and validation of these observations, profiles of tangential velocity and temperature across the liquid film thickness, downstream of jet no. 2, are shown in Figs. 10 and 11, respectively. Profiles are extracted in the plane $x = 0$, at two angles $\theta - \theta_2 = -0.13$ and -0.28 rad, with an extra angle $\theta - \theta_2 = 0$ rad for the temperature profile (corresponding to the impinging point of jet no. 2). Regarding the tangential velocity profiles in Fig. 10, all grids give similar results, with a slight difference for the coarsest grid $\Delta_{min} = 300$ μm. The effect of the grid resolution is more pronounced for the temperature profiles. Only the finest grid $\Delta_{min} = 35$ μm allows to have one cell within δ_t in the stagnation zone (Fig. 11(a)), and a reasonable resolution of 5 cells within δ_t at $\theta - \theta_2 = -0.13$ rad, which seems enough for a reasonable prediction of wall heat flux. Further away from the stagnation zone, at $\theta - \theta_2 = -0.28$ rad, both grids $\Delta_{min} = 35$ and 100 μm give similar results. The resolution of the two coarser grids clearly does not allow to capture finely the temperature profiles, whichever the location considered here, which explains the incorrect prediction of heat transfer. Finally, by comparing Figs. 10 and 11, it is interesting to note the impact of the high Pr number of the liquid, as it clearly appears than the hydrodynamic boundary layer δ is larger than the thermal boundary layer δ_t. For the two locations considered, δ has even reached the film thickness.

3.5. Film characterization

Although the grid sensitivity analysis carried out in this study shows elements of grid convergence for both hydrodynamics and heat transfer, further analysis of the film flow is necessary. The film in the present simulations is characterized in terms of local film height H_{film} and film velocity u_{film}, defined as the tangential velocity averaged over the film thickness. Averaged over the end-windings, film characteristics are similar for the outer and inner surfaces (see Table 7), with slightly lower values for the side surface. On average, $\overline{H}_{film}$ on the side surface

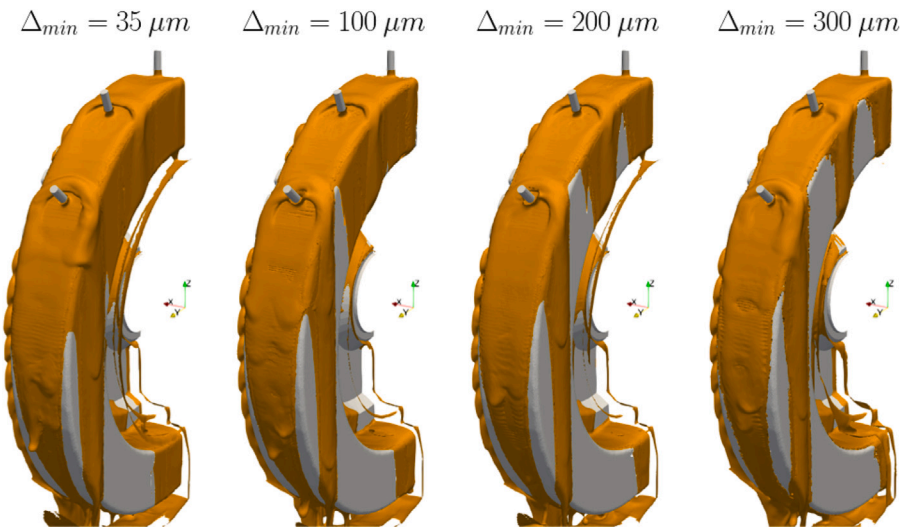

Fig. 8. Iso-contour of void fraction $\alpha = 0.5$ for the 4 b.–l. grids, at $t = 5$ s for $\Delta_{min} = 100$, 200 and 300 µm, and at $t = 10$ s for $\Delta_{min} = 35$ µm.

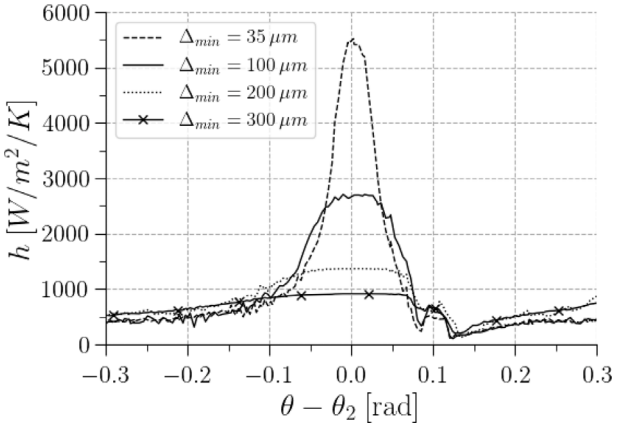

Fig. 9. Evolution of HTC with θ for jet no. 2, in the plane $x = 0$.

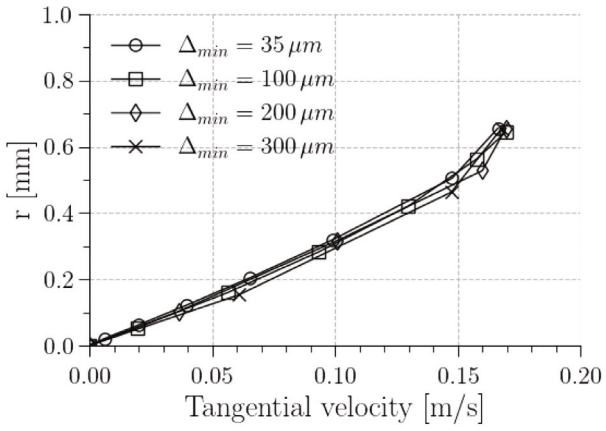

(a) $\theta - \theta_2 = -0.13$ rad

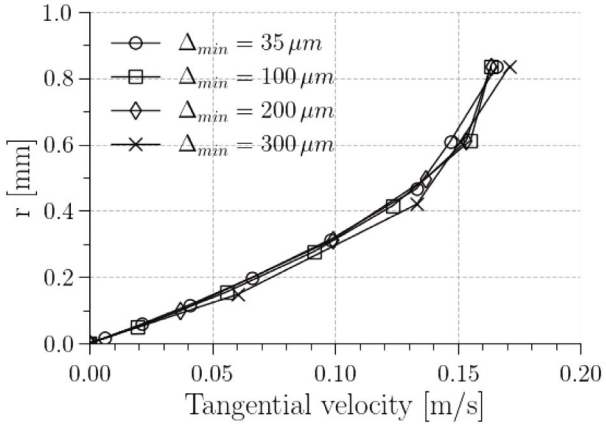

(b) $\theta - \theta_2 = -0.28$ rad

Fig. 10. Profiles of tangential velocity within the liquid film thickness, normal to the outer surface, at two locations in the plane $x = 0$: $\theta - \theta_2 = -0.13$ and -0.28 rad. Markers represent cell centers.

is 0.59 mm, against 1.15 and 1.55 for the outer and inner surface, respectively. Given the 0.4 mm thickness of the b.–l. grid, it means most of the film lays within the b.–l. grid, which could make it more sensitive to the b.–l. grid resolution. This observation may explain the decrease in wet surface with the b.–l. grid resolution observed exclusively on the side surface (Fig. 8 and Table 6).

For grid $\Delta_{min} = 35$ µm, the average film Reynolds number $\overline{Re}_{film} = \overline{u}_{film}\overline{H}_{film}/\nu_f$ ranges between 6 for the side surface to 18.4 for the inner surface, with an average of 13 over the entire film (with however a wide standard deviation of 17). The distribution of Re_{film} for the film formed over the entire surface of end-windings for all four b.–l. grids is shown in Fig. 12. Very little difference can be noticed between the grids, which is confirmed by average values of $\overline{u}_{film}$, $\overline{H}_{film}$ and $\overline{Re}_{film}$ for all 4 grids in Table 7. Most of the film locally has small Reynolds number, with 75% of local Re_{film} being under 18.4. This film description applies only to the reference operating conditions. Simulations described in Section 4 extend this description to other operating conditions.

3.6. Summary and discussion

For the reference operating conditions considered in this section, the grid strategy combining AMR at the gas/liquid interface and a boundary-layer grid on the end-windings seems relevant to capture both film hydrodynamics and heat transfer for a manageable computational time. Refining the AMR cell size lower than 0.3 mm is found to increase considerably the computational time, without impacting significantly the flow hydrodynamics, therefore the AMR cell size is

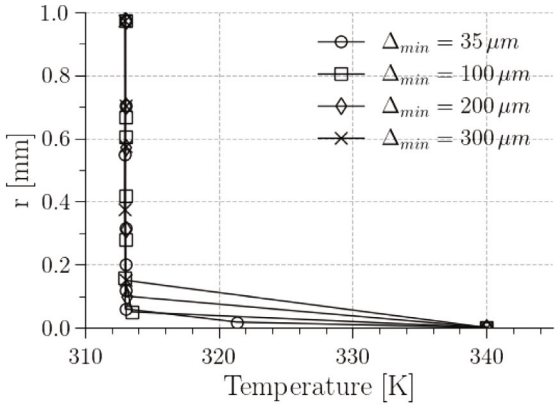

(a) $\theta - \theta_2 = 0$ rad

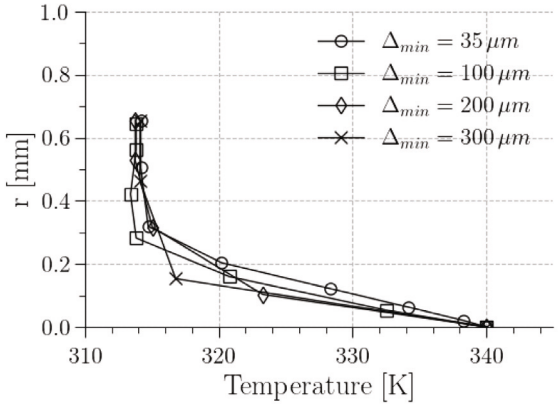

(b) $\theta - \theta_2 = -0.13$ rad

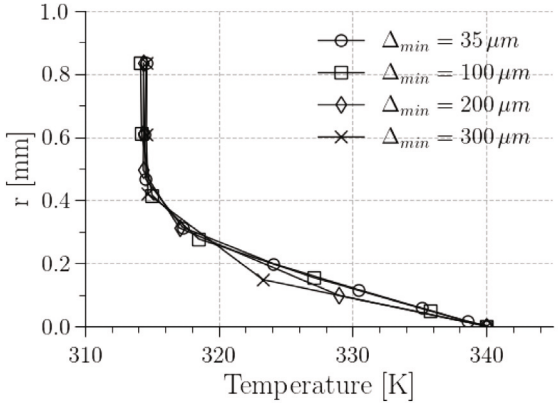

(c) $\theta - \theta_2 = -0.28$ rad

Fig. 11. Profiles of temperature within the liquid film thickness, normal to the outer surface, at three locations in the plane $x = 0$: $\theta - \theta_2 = 0$, −0.13 and −0.28 rad. Markers represent cell centers.

kept at a constant value of 0.3 mm. The film hydrodynamics (wetting, film velocity and film thickness) is found to be little sensitive to the 4 b.–l. grids tested here. Indeed, the coarsest b.–l. grid with an off-wall cell size of 0.3 mm, combined to the AMR cell size of 0.3 mm as well, ensures a minimal resolution of 4 cells within the average film thickness of 1.2 mm, which seems enough to obtain relevant results.

Regarding heat transfer, only the finest b.–l. grid Δ_{min} = 35 µm is able to give accurate predictions in the jets impingement zones, where the thermal boundary layer is the thinnest. However, for the present configuration, given the small number of jets, these areas represent a

Table 7
Average and standard deviation values for film height, velocity and Reynolds number, for ref. operating conditions.

Δ_{min}	End-windings	H_{film} (mm)		u_{film} (m s^{-1})		Re_{film}	
(µm)	surface	Average	Std. dev.	Average	Std. dev.	Average	Std. dev.
35	Outer	1.15	0.88	0.13	0.11	12.2	17.9
	Inner	1.55	0.75	0.17	0.12	18.4	16.4
	Side	0.59	0.47	0.09	0.1	6.0	10.7
	Total	1.22	0.85	0.13	0.12	13.2	17.1
100		1.27	0.83	0.13	0.11	13.1	16.0
200	Total	1.28	0.82	0.14	0.12	14.1	17.5
300		1.22	0.84	0.13	0.12	12.3	16.4

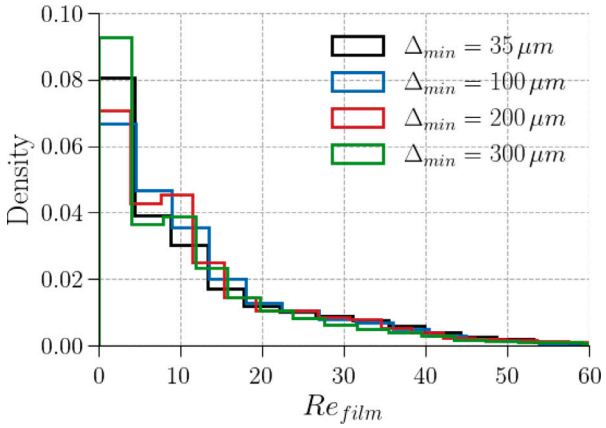

Fig. 12. Distribution of Re_{film} for the film formed on the whole surface of end-windings for ref. operating conditions.

limited amount of the total cooling. This is why the coarser b.–l. grid Δ_{min} = 100 µm over-predicts average heat transfer coefficient $\overline{h}$ by only 6% over the end-windings.

Finally, spreading of the film is twice as slow for b.–l. grid Δ_{min} = 35 µm as for other grids, probably due to the moving contact line modeling, as explained in Section 3.3. Future work should aim at reducing this grid sensitivity, which leads for the present simulation to a doubling of the computational time. For the present study, considering the limited error induced by the b.–l. grid Δ_{min} = 100 µm on the film hydrodynamics and heat transfer, it was chosen (along with an AMR cell size fixed at 0.3 mm) to investigate the impact of oil properties and oil flow rate.

4. Impact of oil properties and oil flow rate on cooling

As previously described in Section 2.2, a variation of oil flow rate and oil properties is carried out to study their impact on hydrodynamics and heat transfer (see Table 2). When available, qualitative comparisons with measurements performed on this machine [7], or with relevant studies from the literature, are provided. These simulations are also intended to extend the ranges of film properties described in Section 3.5 (Re_{film}, H_{film}) for the reference operating conditions. These statistics are summarized in Table 8.

As mentioned in Section 3.6, the grid applied for all parametric variations in this section uses AMR at the liquid/air interface with a fixed cell size of 0.3 mm, and the b.–l. grid Δ_{min} = 100 µm as defined in Table 4. It was seen in Section 3.4 that this grid leads to a mis-prediction of heat transfer in the jet impingement areas, because $\Delta_{min} > \delta_{t,stagn}$, without leading to large errors in prediction of heat transfer over the end-windings (less than 10%). Among the variations considered here, only the increase in liquid flow rate and the decrease in oil viscosity, carried out in Sections 4.1 and 4.2, respectively, entail a decrease in $\delta_{t,stagn}$, then a potential increase in the error on heat

Table 8
Average and standard deviation values over the end-windings for film height, velocity and Reynolds number, for all operating conditions.

Parameter		H_{film} (mm)		u_{film} (m s^{-1})		Re_{film}	
		Average	Std. dev.	Average	Std. dev.	Average	Std. dev.
$\dot{v}$ (l min^{-1})	1.8	1.28	0.78	0.139	0.12	13.9	17.5
	2.85[a]	1.27	0.83	0.135	0.11	13.1	16.0
	5	1.44	0.96	0.183	0.16	18.7	21.6
	8	1.70	1.17	0.260	0.26	27.7	29.0
ν_f (mm^2 s^{-1})	8.5	1.19	0.82	0.170	0.12	26.5	31.0
	15[a]	1.27	0.83	0.135	0.11	13.1	16.0
	32	1.54	0.94	0.118	0.11	6.4	8.3
	f(T)	1.24	0.83	0.165	0.12	22.3	24.6
σ (N m^{-1})	0.02	1.24	0.82	0.142	0.12	13.3	15.6
	0.025	1.20	0.82	0.130	0.11	12.75	17.34
	0.03[a]	1.27	0.83	0.140	0.11	13.1	16.0
	0.035	1.32	0.85	0.145	0.12	14.5	18.13
	0.04	1.38	0.92	0.152	0.12	15.9	21.9
θ_s (°)	10	1.27	0.84	0.130	0.10	12.9	16.7
	30[a]	1.27	0.83	0.135	0.11	13.1	16.0
	60	1.35	0.87	0.138	0.12	13.4	17.4
	90	1.47	0.82	0.155	0.13	16.1	21.4
	120	1.56	0.87	0.159	0.15	17.8	23.6

[a] Reference case.

transfer. Values of $\delta_{t,stagn}$ are however expected to remain in the same order of magnitude as for the reference operating conditions simulated in Section 3. For the highest liquid flow rate considered, $\delta_{t,stagn} \approx 20$ µm, and for the lowest oil viscosity, $\delta_{t,stagn} \approx 30$ µm, against 33 µm for the reference conditions, according to Table 3. The error induced by the grid $\Delta_{min} = 100$ µm on the heat transfer predictions should then remain of similar order, around 10%, making it relevant to compare these simulations with one another.

4.1. Impact of oil flow rate

The impact of an increase in oil flow rate on the film forming over the end-windings is illustrated in Fig. 13. First, the film covers a wider part of the side surface. This leads to a slight increase of the overall wet surface ratio as the liquid flow rate increases, from 0.71 to 0.87 in Fig. 14. The increase from 5 to 8 l min^{-1} has almost no further impact on ξ. Instead, film is formed elsewhere (rotor, casing), which is not necessarily desired as it will not contribute to the cooling of the end-windings. The interactions between the impinging jets differ, with the recirculation zones moving upstream of each jet as the flow rate increases. Enhanced heat transfer due to the film $\overline{h}_{film}$ can be noticed in Fig. 14, which is expected as $\overline{Re}_{film}$ increases with the flow rate (for $\dot{v} \geq 2.85$ l min^{-1}): from 13 ($\dot{v} = 2.85$ l min^{-1}) to 28 ($\dot{v} = 8$ l min^{-1}), with $\overline{u}_{film}$ getting multiplied by 2 and $\overline{H}_{film}$ by 1.3 (see Table 8). The increase in $\overline{h}_{film}$ with flow rate is also due to a greater contribution from the cooling due to the impinging jets, linked to the increase in Re_j [13,29]. Consequently, value of $\overline{h}_{film}$ over the end-windings rises by 54% when increasing liquid flow rate from 1.8 to 8 l min^{-1}. Combined to the slight improvement in wet surface ratio, this logically leads to an increase in surface-average HTC $\overline{h}$ of 78% (Fig. 14).

Previous numerical studies found a similar impact of film flow rate on wetting [30,31] and on film height and film velocity [30]. Experimentally, an improvement of the cooling of the electric machine was measured for the same cooling system (5 impinging jets), but for a higher oil temperature (333 K instead of 313 K), when increasing the oil flow rate from 4 to 8 l min^{-1} [7]. Previous experiments also found enhanced cooling with increasing flow rate for various oil injection systems [32], and for hairpin end-windings [9].

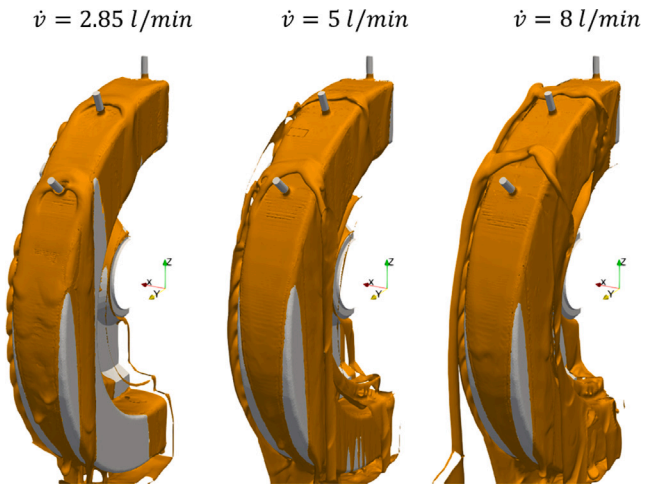

Fig. 13. Iso-contour of void fraction $\alpha = 0.5$ for three oil flow rates, at $t = 5$ s for $\dot{v} = 2.85$ l min^{-1} and $t = 4$ s for $\dot{v} = 5$ and 8 l min^{-1}.

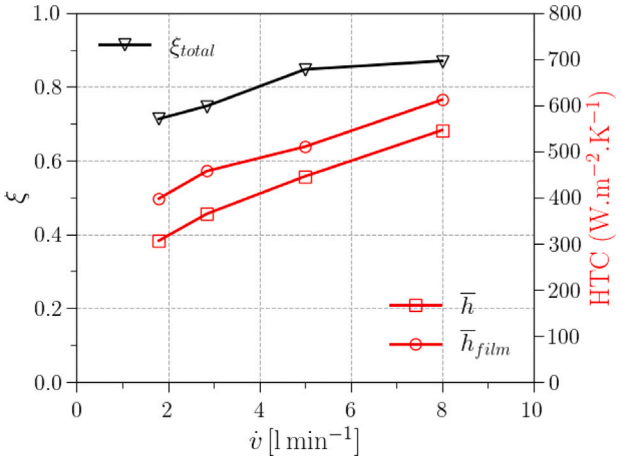

Fig. 14. Steady-state wet surface ratio and surface-averaged HTC for a variation of oil flow rates.

4.2. Impact of oil viscosity

4.2.1. Fixed value of viscosity

The sensitivity of the film to a variation of liquid viscosity is illustrated in Fig. 15. The increase in viscosity considered here affects particularly the wetting on the side surface of the end-windings. Over the entire end-windings, this only leads to a slight increase in wet surface ratio ξ, from 0.68 to 0.77 in Fig. 16, as the inner surface wetting is reduced for the highest viscosity. An improved film spreading at a higher viscosity was also found in experiments and simulations of falling film on an inclined plate [24]. Locally, the film gets thicker with a higher viscosity, and the mean film velocity decreases by a similar extent to conserve the imposed flow rate (see Table 8). The increase in viscosity causes antagonist effects on heat transfer: a decrease in $\overline{Re}_{film}$ (from 26.5 to 6.4 according to Table 8), which should decrease heat transfer, as well as an increase in Pr (107 to 396 in Table 3), which should have the contrary effect. Here, the decrease in $\overline{Re}_{film}$ clearly prevails, causing a lower cooling efficiency of the film (−35% in $\overline{h}_{film}$ between the min. and max. viscosity tested here, in Fig. 16), which logically translates into lower average HTC $\overline{h}$ (−30%), despite the slight increase in wet surface ratio mentioned previously. Experimentally, 4 different oils were tested, with values of ν_f at 313 K ranging from 7 to 26 mm^2 s^{-1}. The cooling system, however, was a flat jet nozzle, which considerably differs from the present configuration.

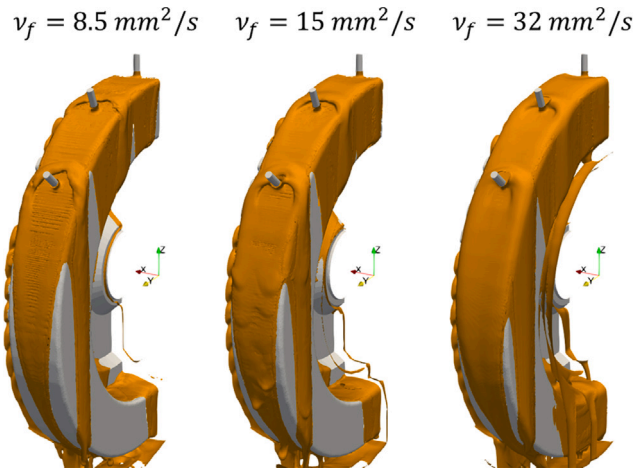

Fig. 15. Iso-contour of void fraction $\alpha = 0.5$ for three values of ν_f, at $t = 5$ s.

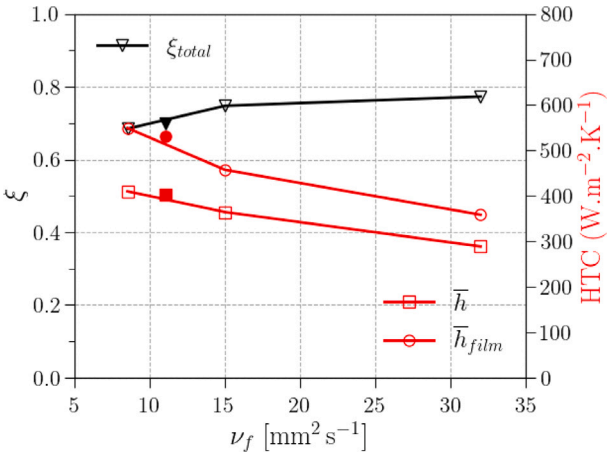

Fig. 16. Steady-state wet surface ratio (a) and surface-averaged HTC (b) for a variation of viscosity ν_f. For the case $\nu_f = f(T)$, symbols (▼), (■) and (●) denote the values of ξ, $\overline{h}$ and $\overline{h}_{film}$ for the total end-windings surface, respectively. These values are given at $\nu_f = 11$ mm^2 s^{-1}, corresponding to the viscosity at the average temperature of the film.

A slightly degraded cooling was measured when considering more viscous oils, which qualitatively agrees with the present results. Other experimental works found a similar impact of the oil viscosity for hairpin end-windings [33].

4.2.2. Variation of viscosity with oil temperature

So far, the oil viscosity was considered a constant value in the simulations. In reality, this type of liquid can present a strong variation of the viscosity with the temperature. Thus, the oil injected at temperature T_f is expected to be heated up close to the wall at a temperature $T > T_f$, decreasing the viscosity locally in the film. To investigate this impact, the case with a constant viscosity $\nu_f = 15$ mm^2 s^{-1} is compared to a simulation performed with a temperature-variable viscosity $\nu_f = f(T)$ defined in Eq. (1) in Section 2.2. To only account for the effect due to the film heat-up, the constant C in Eq. (1) is imposed so that $\nu_f(T = T_f) = 15$ mm^2 s^{-1}. Varying the viscosity with temperature leads to a slight decrease in wet surface ratio ($\xi = 0.70$ compared to 0.75 in Fig. 16), an increase in $\overline{h}_{film}$ (+16%) and $\overline{h}$ (+10%) according to Fig. 16. This is in line with the behavior observed in Section 4.2.1: as the film heats up with increasing distance from the jet impingement areas, its viscosity decreases significantly. The film, therefore, becomes progressively thinner and accelerates so that the mean flow rate is conserved. This effect was characterized experimentally for falling liquid-films on an inclined plate for similar Reynolds and Prandtl numbers in [34]. The resulting average temperature of the film is 322 K, which allows to estimate the average viscosity of the film to 11 mm^2 s^{-1}, based on Eq. (1). This is 25% lower than the reference case. Logically, resulting film characteristics, wet surface ratio and HTC rank between the results obtained with $\nu_f = 8.5$ and 15 mm^2 s^{-1} in Table 8 and Fig. 16. These results show the importance of accounting for the variation of viscosity with temperature when performing this type of simulations, even though it entails a specific experimental characterization of the oil.

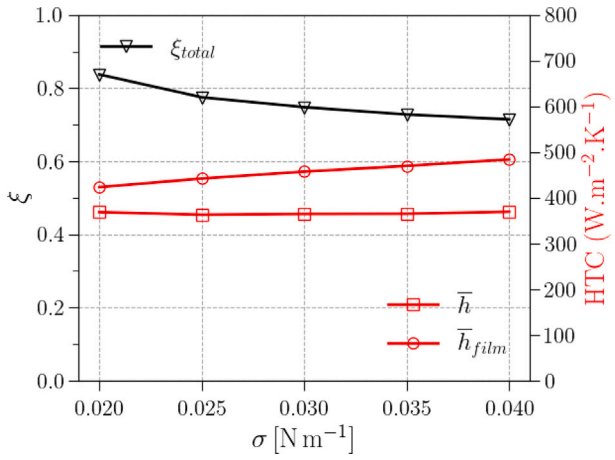

Fig. 17. Steady-state wet surface ratio and surface-averaged HTC for a variation of oil surface tension.

4.3. Surface tension

The variation of surface tension performed here has a limited impact on the film. With a higher surface tension, the film slightly shrinks on the outer and side surfaces, leading to a decrease in ξ of 14.7% on the end-windings when the surface tension increases from 0.02 to 0.04 N m^{-1}, as indicated in Fig. 17. This lower wet surface ratio as the surface tension increases does not translate into a lower HTC $\overline{h}$, which remains quasi constant. Indeed, the cooling efficiency of the film improves for a higher surface tension (+14% on $\overline{h}_{film}$ when σ increases from 0.020 to 0.04 N m^{-1}). This is due to an increase in average film height $\overline{H}_{film}$ (from 1.24 to 1.38 mm in Table 8), leading to a higher $\overline{Re}_{film}$ (from 13.3 to 15.9). These effects of surface tension on both film shrinkage and film height were observed in previous studies [30,35].

4.4. Contact angle

The film resulting from a variation of the static contact angle θ_s, from hydrophilic ($\theta_s = 10°$) to hydrophobic values ($\theta_s = 120°$), is shown in Fig. 18. Wetting dramatically deteriorates as the contact angle increases. Film detachment is visible on the lower part of the outer surface, and on the side surface, the film reduces to thin rivulets. These observations are confirmed by the evolution of wet surface ratio with θ_s plotted in Fig. 19: over the end-windings, ξ falls from 0.91 for $\theta_s = 10°$ down to 0.25 for $\theta_s = 120°$. This film shrinkage is associated to an increase in film thickness $\overline{H}_{film}$, from 1.27 mm to 1.56 mm for $\theta_s = 10°$ and 120°, respectively (see Table 8). Both aspects were observed in previous studies, for instance in simulations and experiments of film falling on an inclined plate [35], or in simulations of a film falling over a horizontal tube [36–38]. In the present simulations, the average film velocity $\overline{u}_{film}$ is also found to increase in the same proportion as the average film height, leading to a slightly higher $\overline{Re}_{film}$ (from 12.9 to 17.8 according to Table 8). The drop in wet surface consequently

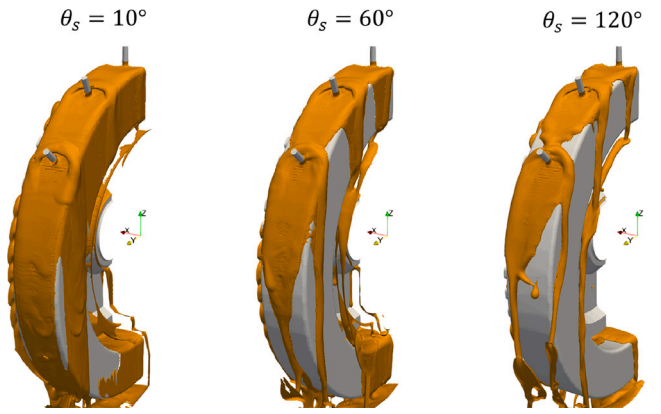

Fig. 18. Iso-contour of void fraction $\alpha = 0.5$ for three values of static contact angle θ_s, at $t = 5$ s for $\theta_s = 10$ and 60 and $t = 4$ s for $\theta_s = 120°$.

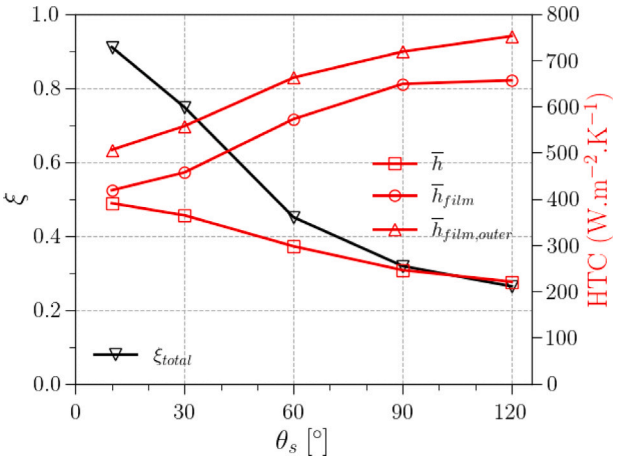

Fig. 19. Steady-state wet surface ratio and surface-averaged HTC for a variation of static contact angle.

leads to a decrease in surface-average HTC $\overline{h}$ over the end-windings, as illustrated in Fig. 19, and also observed in previous studies [38,39]. However, this decrease is not proportional to that of the wet surface ratio ξ. Indeed, the cooling efficiency of the film improves with the contact angle: in Fig. 19, $\overline{h}_{film}$ increases by 61% between $\theta_s = 10°$ and $\theta_s = 120°$. The limited increase in $\overline{Re}_{film}$ mentioned previously cannot entirely explain this effect. As θ_s increases, the film concentrates on the outer surface, where the film cooling $\overline{h}_{film,outer}$ is higher due to the impinging jets. This can be quantified by the ratio of film on the outer surface over the total film surface $S_{film,outer}/S_{film}$, defined as:

$$\frac{S_{film,outer}}{S_{film}} = \frac{\xi_{outer}\, S_{outer}}{\xi\, S_{total}} \tag{18}$$

For $\theta_s = 30°$, this ratio is 0.4. It almost linearly increases to reach 0.61 for $\theta_s = 120°$. In addition, the efficiency of the film cooling on the outer surface increases with θ_s, as illustrated by the evolution of $\overline{h}_{film,outer}$ in Fig. 19. Indeed, as the film on the outer surface tends to shrink as well, the proportion of the cooling due to the impinging jet areas increases.

4.5. Summary and discussion

Over all parametric variations tested here, the average film Reynolds $\overline{Re}_{film}$ does not exceed 30 (for cases of low viscosity or high flow rate), with a standard deviation of similar magnitude. Overall, local Re_{film} rarely exceeds 100. Film height remains on average between 1.2 and 1.6 mm, but again with a high standard deviation, 0.8–0.9 mm.

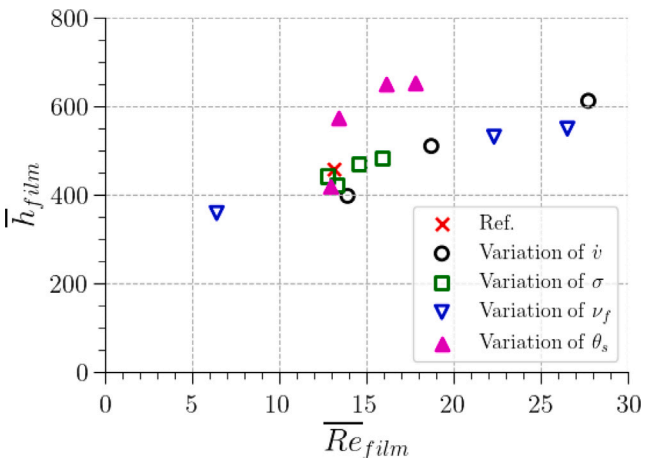

Fig. 20. Values of $\overline{h}_{film}$ as a function $\overline{Re}_{film}$ for the parametric variations.

The study of the impact of some of the oil properties and oil flow rate reveals the importance of local film characterization to explain the variations in heat transfer. Indeed, as long as the wet surface ratio is only slightly impacted, as it is the case for the variations of oil flow rate, oil viscosity and surface tension performed in Sections 4.1–4.3 respectively, heat transfer due to the film can be correlated to the average film height and/or film velocity. This is illustrated in Fig. 20, depicting an almost linear relation between $\overline{h}_{film}$ and $\overline{Re}_{film}$ for the operating conditions corresponding to these 3 variations. It should be noted that $\overline{h}_{film}$ is also expected to increase with the Prandtl number [19,29], which varies here over only four operating conditions (the viscosity variation), at the same time as $\overline{Re}_{film}$. Therefore the present results do not allow to highlight this effect. Regarding the variation of contact angle θ_s, film features (and particularly wetting) change too radically for $\overline{h}_{film}$ to depend only on $\overline{Re}_{film}$, as explained in Section 4.4. This is why these 4 points deviate from the others in Fig. 20. Finally, this numerical approach can help to define optimum cooling conditions, which are based on a compromise between the oil's intrinsic properties, oil temperature (which determines its viscosity), pumping losses, and so on. For example, it is found here that an oil with low viscosity can form a film that is just as cooling as an increase in flow rate. The present results also confirmed the necessity to evaluate the oil properties and to take them into account in numerical works, for accurate predictions of film flows and heat transfer.

5. Conclusions

Two-phase flow simulations of the direct liquid cooling of the end-windings of a realistic electric machine were carried out using the VoF approach. Simplifying assumptions were adopted to reduce the complexity of the flow as well as the computational cost. This made it possible to perform a large number of simulations to characterize the liquid jets and film hydrodynamic and heat transfer, with the objective to provide elements of validation and understanding in the absence of experimental measurements. To the best of the authors' knowledge, such an analysis for this type of flow, on this industrial scale, has never been carried out in the literature. The study was carried out in two main stages. First, a grid sensitivity study was conducted considering fixed flow conditions, in order to validate the numerical setup in the absence of direct experimental data. The grid strategy chosen here (AMR for liquid/gas interface and boundary-layer grid) yields hydrodynamic characteristics, such as wet surface ratio and film Reynolds number, that are little sensitive to variations in cell size. However, the large Prandtl numbers of the liquid considered here impose a relatively fine grid to correctly predict heat transfer,

particularly in the jet impingement areas. A thorough study of heat transfer in this last region showed that a grid convergence could be achieved for the finest boundary-layer grid tested. However, due to the limited contribution of the jet impingement zones to the overall cooling compared to the rest of the film, a coarser grid, with a minimum cell height of 100 μm at the wall, was found to induce a limited error on heat transfer prediction over the entire cooled surface (less than 10%) while reducing significantly the computational cost.

Secondly, variations of liquid flow rate and liquid properties were carried out. Again, hydrodynamics and heat transfer were characterized. The resulting trends compared qualitatively well to previous numerical of experimental work in the literature. A wider film was obtained by increasing the liquid flow rate or the viscosity, or by decreasing the surface tension or the static contact angle (this last parameter being the most sensitive, for the range of values tested). However, a higher wet surface ratio did not necessarily lead to an increase in overall heat transfer on the end-windings. Only an increase in liquid flow rate led to a larger wet surface and thus to a more efficient film cooling. However, when the other three properties are varied, the film cooling efficiency deteriorates despite the increase in the wet surface, which led to contrasted outcomes: a decrease in heat transfer when increasing the viscosity, a increase in heat transfer when decreasing the static contact angle, or unchanged heat transfer when decreasing surface tension. These variations can be significant (viscosity or contact angle in particular), which shows the necessity to evaluate accurately these properties.

The analysis of all simulations showed that the average film Reynolds number does not exceed 30, with average film height between 1.2 and 1.6 mm. These statistics are useful to carry out future experiments and/or simulations of falling liquid film, in relevant operating conditions, to further validate the numerical approach. Future work will also focus on the validation of a dynamic contact angle model, to reduce the sensitivity of the transient flow to the grid cell size along the wall. It will be also interesting to carry out thermal simulations of the electric machine, to evaluate the sensitivity of heat transfer uncertainty related to grid coarsening on the prediction of end-windings temperature, and further validate the use of an intermediate boundary-layer grid in the present study. Finally, the numerical set-up should be completed to account for the impact of rotor movement on the liquid film, as well as the effect of the corrugated surface of the end-windings.

CRediT authorship contribution statement

Adèle Poubeau: Writing – original draft, Visualization, Methodology, Formal analysis, Conceptualization. **Guillaume Vinay:** Writing – review & editing, Supervision, Conceptualization. **Breno Mendes Alves:** Writing – review & editing, Methodology, Conceptualization. **Xiaohan Bai:** Writing – review & editing, Methodology, Conceptualization. **Pierre Viot:** Writing – review & editing, Methodology, Conceptualization.

Declaration of competing interest

The authors declare that they have no known competing financial interests or personal relationships that could have appeared to influence the work reported in this paper.

Data availability

Data will be made available on request.

Acknowledgments

The numerical part of the work was carried out and funded at IFPEN, France as part of an internal research project. All calculations were performed on the IFPEN supercomputer.

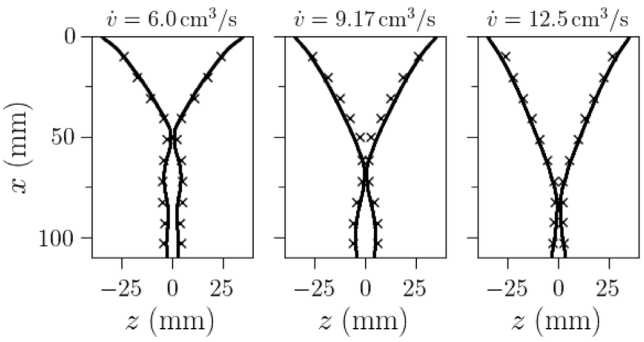

Fig. A.21. Contact lines of the film at equilibrium state for the three volumetric flow rates, obtained experimentally (×) in [24] and numerically (–).

Appendix. Simulation of falling liquid films with side contact lines on a flat plate

To validate the numerical solver for liquid film simulations, the experimental setup by Thoraval et al. [24], designed to characterize a falling film of a partially wetting fluid, was reproduced numerically. In this experiment, the liquid is injected through a rectangular slot of width 70 mm, forming a film which falls down a vertical flat plate. The film is not in contact with sidewalls: surface tension effects causes the film to contract in the spanwise direction. Among all the cases considered in this study, a variation of volumetric flow rate (6, 9.17 and 12.5 $\mathrm{cm}^3\ \mathrm{s}^{-1}$) is numerically reproduced for a water/glycerol mixture (60%). The numerical models are similar to those defined in Section 2.4, with a static contact angle fixed at $\theta_s = 82°$ (experimentally, it was found to range between 69 and 82°). A uniform flow rate is imposed at the inlet located at $x = 0$, the film falls down in the x-direction (y and z being the wall-normal and the spanwise directions, respectively). The grid is refined in the film to ensure a minimal resolution of 7 cells within the film thickness ($\Delta_y = 80$ μm, $\Delta_{x,z} = 3\Delta_y$).

Fig. A.21 compares the position of the contact lines of the film for equilibrium state obtained experimentally in [24] and numerically. The flow converges into a single rivulet under the effect of surface tension forces, and the onset of the rivulet moves downstream as the flow rate increases, increasing the wet surface. For all three values of flow rate, simulations compare very well to the experimental results.

References

[1] Q. Lu, R. Muthukumar, H. Ge, S. Parameswaran, Numerical study of a rotating liquid jet impingement cooling system, Int. J. Heat Mass Transfer 163 (2020) 120446, http://dx.doi.org/10.1016/j.ijheatmasstransfer.2020.120446.

[2] H. Xu, K. Lin, C. Ehrenpreis, G. Roux, R.W. de Doncker, Thermal modeling of electrical machines with advanced fluid cooling, in: 2020 19th IEEE Intersociety Conference on Thermal and Thermomechanical Phenomena in Electronic Systems (ITherm), IEEE, 2020, pp. 491–496.

[3] C. Srinivasan, X. Yang, J. Schlautman, D. Wang, S. Gangaraj, Conjugate heat transfer CFD analysis of an oil cooled automotive electrical motor, in: SAE Technical Paper Series, in: SAE Technical Paper Series, SAE International400 Commonwealth Drive, Warrendale, PA, United States, 2020, http://dx.doi.org/10.4271/2020-01-0168.

[4] C. Srinivasan, J. Wan, R. Saha, S. Dhar, K. Paciura, S. Zhu, V. Nichani, R. Ranganathan, Heat transfer analysis of an electric motor cooled by a large number of oil sprays using computational fluid dynamics, in: SAE Technical Paper Series, in: SAE Technical Paper Series, SAE International400 Commonwealth Drive, Warrendale, PA, United States, 2022, http://dx.doi.org/10.4271/2022-01-0208.

[5] R.O. Grover, X. Yang, S. Parrish, L. Nocivelli, K.J. Asztalos, S. Som, Y. Li, C. Burns, J. van Gilder, N. Attal, O. Avanessian, CFD simulations of electric motor end ring cooling for improved thermal management, Sci. Technol. Energy Transit. 77 (2022) 17, http://dx.doi.org/10.2516/stet/2022015.

[6] T. Davin, J. Pellé, S. Harmand, R. Yu, Experimental study of oil cooling systems for electric motors, Appl. Therm. Eng. 71 (1) (2014) 607, http://dx.doi.org/10.1016/j.applthermaleng.2014.05.021.

[7] R. Sindjui, G. Zito, S. Zhang, Experimental study of systems and oils for direct cooling of electrical machine, J. Therm. Sci. Eng. Appl. 14 (5) (2021) http://dx.doi.org/10.1115/1.4051934.
[8] T. Ha, Y. Kang, N.S. Kim, S.H. Park, S.H. Lee, D.K. Kim, H.S. Ryou, Cooling effect of oil cooling method on electric vehicle motors with hairpin winding, J. Mech. Sci. Technol. 35 (1) (2021) 407–415, http://dx.doi.org/10.1007/s12206-020-1240-y.
[9] T. Ha, D.K. Kim, Study of injection method for maximizing oil-cooling performance of electric vehicle motor with hairpin winding, Energies 14 (3) (2021) 747, http://dx.doi.org/10.3390/en14030747.
[10] D.H. Lim, S.C. Kim, Thermal performance of oil spray cooling system for in-wheel motor in electric vehicles, Appl. Therm. Eng. 63 (2) (2014) 577–587, http://dx.doi.org/10.1016/j.applthermaleng.2013.11.057.
[11] Z. Liu, T. Winter, M. Schier, Direct coil cooling of a high performance switched reluctance machine (SRM) for EV/HEV applications, SAE Int. J. Altern. Powertrains 4 (1) (2015) 162–169, http://dx.doi.org/10.4271/2015-01-1209.
[12] A. Pandey, B. Madduri, C.-Y. Perng, C. Srinivasan, S. Dhar, Multiphase flow and heat transfer in an electric motor, in: Proceedings of ASME 2022 International Mechanical Engineering Congress and Exposition, IMECE2022, The American Society of Mechanical Engineers, New York, N.Y., 2022, http://dx.doi.org/10.1115/IMECE2022-96801.
[13] A. Poubeau, G. Vinay, B. Kekelia, K. Bennion, Numerical simulations of high Prandtl number liquid jets impinging on a flat plate, Int. J. Heat Mass Transfer 205, 123889, http://dx.doi.org/10.1016/j.ijheatmasstransfer.2023.123889.
[14] A. Waikar, D. Rowinski, A. Dahale, Conjugate heat transfer modeling of oil jet impingement cooling on corrugated wire surfaces, in: ILASS-Americas 33rd Annual Conference on Liquid Atomization and Spray Systems, Albuquerque, New Mexico, 2023.
[15] R.S. Brodkey, The Phenomena of Fluid Motions, Addison-Wesley, Reading, MA, 1967.
[16] S.P. Kemp, J.L. Linden, Physical and Chemical Properties of a Typical Automatic Transmission Fluid, Tech. rep., Society of Automotive Engineers, Warrendale, PA (USA), 1990.
[17] K.J. Richards, P.K. Senecal, E. Pomraning, CONVERGE 3.1.6, 2023.
[18] C.F. Ma, Q. Zheng, S.Y. Ko, Local heat transfer and recovery factor with impinging free-surface circular jets of transformer oil, Int. J. Heat Mass Transfer 40 (18) (1997) 4295–4308, http://dx.doi.org/10.1016/S0017-9310(97)00054-9.
[19] C. Renon, M. Fénot, M. Girault, S. Guilain, B. Assaad, An experimental study of local heat transfer using high Prandtl number liquid jets, Int. J. Heat Mass Transfer 180 (2021) http://dx.doi.org/10.1016/j.ijheatmasstransfer.2021.121727.
[20] X. Liu, J.H. Lienhard V, J.S. Lombara, Convective heat transfer by impingement of circular liquid jets, J. Heat Transfer 113 (3) (1991) 571–582, http://dx.doi.org/10.1115/1.2910604.
[21] C. Hirt, B. Nichols, Volume of fluid (VOF) method for the dynamics of free boundaries, J. Comput. Phys. 39 (1) (1981) 201–225, http://dx.doi.org/10.1016/0021-9991(81)90145-5.
[22] S. Muzaferija, M. Peric, P. Sames, T. Schelin, A two-fluid Navier-Stokes solver to simulate water entry, in: Proceeding of 22nd Symposium on Naval Hydrodynamics, 1998, pp. 638–651.
[23] J.U. Brackbill, D.B. Kothe, C. Zemach, A continuum method for modeling surface tension, J. Comput. Phys. 100 (1992) 335–354.
[24] B. Thoraval, J. Lallement, P. Berthoumieu, C. Laurent, P. Gajan, An experimental study on gravity-driven film: influence of viscosity, wall surface treatment and transitory state, in: 10th International Conference on Multiphase Flow, ICMF, Rio de Janeiro, Brazil, 2019.
[25] C. Huh, L. Scriven, Hydrodynamic model of steady movement of a solid/liquid/fluid contact line, J. Colloid Interface Sci. 35 (1) (1971) 85–101, http://dx.doi.org/10.1016/0021-9797(71)90188-3.
[26] S. Afkhami, S. Zaleski, M. Bussmann, A mesh-dependent model for applying dynamic contact angles to VOF simulations, J. Comput. Phys. 228 (15) (2009) 5370–5389, http://dx.doi.org/10.1016/j.jcp.2009.04.027.
[27] D. Legendre, M. Maglio, Comparison between numerical models for the simulation of moving contact lines, Comput. & Fluids 113 (2015) 2–13, http://dx.doi.org/10.1016/j.compfluid.2014.09.018.
[28] R.G. Cox, The dynamics of the spreading of liquids on a solid surface. Part 1. Viscous flow, J. Fluid Mech. 168 (1986) 169–194, http://dx.doi.org/10.1017/S0022112086000332.
[29] B. Kekelia, K. Bennion, X. Feng, G. Moreno, J.E. Cousineau, S. Narumanchi, J. Tomerlin, Surface temperature effect on convective heat transfer coefficients for jet impingement cooling of electric machines with automatic transmission fluid, in: ASME 2019 International Technical Conference and Exhibition on Packaging and Integration of Electronic and Photonic Microsystems, California, 2019, http://dx.doi.org/10.1115/IPACK2019-6457.
[30] H. Lan, J.L. Wegener, B.F. Armaly, J.A. Drallmeier, Developing laminar gravity-driven thin liquid film flow down an inclined plane, J. Fluids Eng. 132 (8) (2010) http://dx.doi.org/10.1115/1.4002109.
[31] C.H. Qi, H.J. Feng, H.Q. Lv, C. Miao, Numerical and experimental research on the heat transfer of seawater desalination with liquid film outside elliptical tube, Int. J. Heat Mass Transfer 93 (2016) 207–216, http://dx.doi.org/10.1016/j.ijheatmasstransfer.2015.09.043.
[32] T. Davin, J. Pellé, S. Harmand, R. Yu, Experimental study of oil cooling systems for electric motors, Appl. Therm. Eng. 75 (2015) 1–13, http://dx.doi.org/10.1016/j.applthermaleng.2014.10.060.
[33] H. Xu, G.T. Gotz, S. Zhang, R.W. de Doncker, Experimental study of a directly oil-cooled electrical machine for a full-electric vehicle by using low viscosity oil, in: 2022 24th European Conference on Power Electronics and Applications, EPE'22 ECCE Europe, Hanover, Germany, 2022.
[34] A. Charogiannis, C.N. Markides, Spatiotemporally resolved heat transfer measurements in falling liquid-films by simultaneous application of planar laser-induced fluorescence (PLIF), particle tracking velocimetry (PTV) and infrared (IR) thermography, Exp. Therm Fluid Sci. (2019) http://dx.doi.org/10.1016/j.expthermflusci.2018.11.001.
[35] C. Dong, L. Lu, R. Qi, Model development of heat/mass transfer for internally cooled dehumidifier concerning liquid film shrinkage shape and contact angles, Build. Environ. 114 (2017) 11–22, http://dx.doi.org/10.1016/j.buildenv.2016.12.001.
[36] H. Ding, P. Xie, D. Ingham, L. Ma, M. Pourkashanian, Flow behaviour of drop and jet modes of a laminar falling film on horizontal tubes, Int. J. Heat Mass Transfer 124 (2018) 929–942, http://dx.doi.org/10.1016/j.ijheatmasstransfer.2018.03.111.
[37] P. Fernandez de Arroiabe, A. Martinez-Urrutia, X. Peña, M. Martinez-Agirre, M.M. Bou-Ali, Influence of the contact angle on the wettability of horizontal-tube falling films in the droplet and jet flow modes, Int. J. Refrig. 90 (2018) 12–21, http://dx.doi.org/10.1016/j.ijrefrig.2018.04.003.
[38] A. Karmakar, S. Acharya, Wettability effects on falling film heat transfer over horizontal tubes in jet flow mode, J. Heat Transfer 142 (12) (2020) http://dx.doi.org/10.1115/HT2019-3532.
[39] B.H. Kang, K.H. Kim, D.-Y. Lee, Fluid flow and heat transfer on a falling liquid film with surfactant from a heated vertical surface, J. Mech. Sci. Technol. 21 (11) (2007) 1807–1812, http://dx.doi.org/10.1007/BF03177436.